JOURNAL OF AIRCRAFT
Vol. 30, No. 4, July–Aug. 1993

Reynolds Number Effects on Supersonic Asymmetrical Flows over a Cone

J. L. Thomas*
NASA Langley Research Center, Hampton, Virginia 23665

The supersonic viscous flow over a 5-deg half-angle cone at an angle of attack of four times the cone half-angle is studied computationally using both the conical and the three-dimensional Navier-Stokes equations. The numerical solutions were obtained with an implicit, upwind-biased algorithm. Asymmetrical flowfields of the absolute-instability type are found using the conical-flow equations which agree with published results. However, the absolute instabilities of the originally symmetric flow found with the conical equations do not occur in the three-dimensional simulations, although spurious asymmetric three-dimensional flows for symmetric bodies arise if the grid resolution is insufficient in the nose region. The asymmetric flows computed with the three-dimensional equations are convective instabilities and are possible if the local Reynolds number exceeds a critical value and a fixed geometric asymmetry is imposed. A continuous range of asymmetries can be developed, depending on the size of the disturbance and the Reynolds number. As the Reynolds number is increased, the asymmetries demonstrate a bistable behavior at levels of side force consistent with those predicted using the conical equations. Below a certain critical Reynolds number, any flow asymmetries arising from a geometrical asymmetry are damped with increasing distance downstream from the geometrical asymmetry.

Introduction

THE flows over slender bodies at high angles of attack are dominated by lee-side vortices arising from crossflow separations near the nose. These vortices exhibit highly nonlinear interactions with each other and with other components (wings, control surfaces, etc.) and can thereby exert a significant influence on the longitudinal and lateral aerodynamic characteristics of a slender airplane. For bodies symmetric with respect to the longitudinal symmetry plane, the vortical flows are generally steady and symmetric at relatively low angles of attack. With increasing angle of attack, the flowfield becomes asymmetric but remains steady. At larger angles of attack, approaching 90 deg, the flowfields become asymmetric and unsteady and are characterized by unsteady vortex-shedding events associated with the predominantly two-dimensional flow in cross-sectional planes normal to the longitudinal axis of the body.

The phenomena of asymmetrical flow over a symmetric body at high angle of attack has been an intriguing area of interest since it was first revealed on the basis of experimental studies conducted in the 1950s.[1] The onset of asymmetric flow generally occurs at an angle of attack approximately twice the nose half-angle. The observed flow asymmetries are sensitive to slight geometric asymmetries near the nose, such that it is extremely difficult to reproduce experimental results from one test to another, or even from one run to the next during a given experiment.[2–7] Moscovitz et al.[5] and Zilliac[6] found that the asymmetry could be controlled by minute local perturbations to the nose geometry. The effects of increasing either nose bluntness or Mach number are to decrease the asymmetries.

Presented as Paper 91-3295 at the AIAA 9th Applied Aerodynamics Conference, Baltimore, MD, Sept. 23–25, 1991; received Oct. 15, 1991; revision received April 27, 1992; accepted for publication April 27, 1992.

*Head, Computational Aerodynamics Branch, Fluid Mechanics Division, MS 128. Associate Fellow AIAA.

Generally, at angles of attack equal to or slightly greater than that corresponding to the onset of asymmetry, a continuous range of asymmetries are found as the roll orientation of the model, and thereby the geometrical asymmetry of the model nose is changed. At higher angles of attack, the side force tends to change nearly discontinuously with roll orientation, indicating a bistable behavior, although Degani and Tobak[7] have shown experimentally that the variations are actually continuous single-valued variations. At higher angles of attack, $\alpha \geq 65$ deg, the asymmetrical flowfield becomes unsteady and the average side force is reduced in magnitude.

The behavior and origin of the asymmetrical behavior has been the subject of many experimental[1–7] and, more recently, computational studies.[8–15] The nature of the asymmetry is extremely difficult to determine with either computation or experiment, since neither are perfect simulations. For instance, experiments suffer from the inability to manufacture a perfectly symmetric nose tip and freestream nonuniformities. Computations suffer from truncation errors associated with inadequate grid resolution, from convergence difficulties, and from the effects of arithmetic round-off.

Two descriptions for the nature of the observed asymmetries have been put forward. The first is that the asymmetries arise from a hydrodynamic instability similar to that encountered in the wake of the two-dimensional flow past a circular cylinder.[8–13] When the symmetric flow is perturbed asymmetrically, an asymmetry develops and continues even when the initial asymmetry is removed. Thus, asymmetries can be induced by a transient asymmetrical disturbance. This description of the route to asymmetry is referred to as an absolute instability[16] of an initially symmetric flow. Inviscid computations with prescribed separation points on the body support this description as reported in the incompressible small-disturbance calculations by Fiddes[8] and the supersonic Euler computations of Marconi.[9] Also, supersonic laminar computations by Siclari and Marconi,[10] Siclari,[11] and Kandil and Wong[12] have demonstrated asymmetries of the absolute instability type using the approximate conical Navier-Stokes equations. The incompressible three-dimensional turbulent Navier-Stokes computations of Hartwich et al.[13] for a tangent-ogive body at an angle of attack of 40 deg indicate an asymmetric flowfield without the imposition of a fixed geometric asymmetry in the computation. The extent of asymmetry in the computations could be controlled by imposing a geometric

imperfection in the nose region; by imposing asymmetry, excellent agreement with experimentally measured pressures was obtained.[13]

The second description is that the observed asymmetry results from the amplification of a given asymmetry and vanishes if the given asymmetry is removed.[7,14,15] Referred to as a convective-type asymmetry, this point of view is supported by the compressible Navier-Stokes computations of Degani[14,15] for the laminar subsonic flow over a tangent-ogive body at high angle of attack, where steady asymmetries were observed only if a fixed spatial asymmetry was imposed. Removal of the asymmetry always led to a return to symmetric flow. Recently, Degani and Tobak[7] argued on the basis of theory, computation, and experiment that the observed steady asymmetries are convective-type instabilities. There is a generally universal agreement that the unsteady asymmetries observed at angles of attack approaching 90 deg are absolute instabilities.

The type of asymmetry encountered at lower angles of attack, where steady asymmetries are observed, is still in question and is the subject of this investigation. Computations using an implicit, upwind-biased algorithm[17,18] for the Navier-Stokes equations are made for the laminar flow past a 5-deg half-angle circular cone at a supersonic Mach number. A range of Reynolds numbers is considered at an angle of attack of four times the cone half-angle. Only laminar computations are presented here; in the actual physical situation, transition would be expected to occur at the higher of the Reynolds numbers considered herein, and play an important role in the development of the asymmetries. Both locally conical and three-dimensional solutions are computed. The nature of the flowfield which develops over the axisymmetric cone, both with and without imposed geometrical asymmetries in the nose region, is considered. Variations in the grid density are made in order to assess the effects due to truncation errors in the spatial differencing algorithm.

Governing Equations and Numerical Method

The governing equations are the thin-layer approximations to the three-dimensional, time-dependent, compressible Navier-Stokes equations, written in generalized coordinates and conservation law form as

$$\frac{\partial \hat{Q}}{\partial t} + \frac{\partial \hat{F}}{\partial \xi} + \frac{\partial \hat{G}}{\partial \eta} + \frac{\partial (\hat{H} - \hat{H}_v)}{\partial \zeta} = 0 \tag{1}$$

where ζ corresponds to the coordinate normal to the body surface. The conserved variables $\hat{Q}$ represent mass, Cartesian components of momentum, and total energy per unit volume

$$\hat{Q} = (Q/J) = (1/J)\begin{bmatrix} \rho \\ \rho u \\ \rho v \\ \rho w \\ e \end{bmatrix} \tag{2}$$

where $J = \partial(\xi, \eta, \zeta)/\partial(x, y, z)$ is the Jacobian of the steady three-dimensional transformation between the Cartesian coordinates (x, y, z) and the generalized coordinates (ξ, η, ζ). The convective and pressure (Euler) fluxes, $\hat{F}$, $\hat{G}$, $\hat{H}$, and the contravariant components of velocity, U, V, W, are given below:

$$\hat{F} = (1/J)\begin{bmatrix} \rho U \\ \rho U u + \xi_x p \\ \rho U v + \xi_y p \\ \rho U w + \xi_z p \\ (e + p)U \end{bmatrix} \quad \hat{G} = (1/J)\begin{bmatrix} \rho V \\ \rho V u + \eta_x p \\ \rho V v + \eta_y p \\ \rho V w + \eta_z p \\ (e + p)V \end{bmatrix} \tag{3}$$

$$\hat{H} = (1/J)\begin{bmatrix} \rho W \\ \rho W u + \zeta_x p \\ \rho W v + \zeta_y p \\ \rho W w + \zeta_z p \\ (e + p)W \end{bmatrix}$$

$$U = \xi_x u + \xi_y v + \xi_z w$$

$$V = \eta_x u + \eta_y v + \eta_z w \tag{4}$$

$$W = \zeta_x u + \zeta_y v + \zeta_z w$$

The pressure p is defined from the equation of state for an ideal gas

$$p = (\gamma - 1)[e - \rho q^2/2] \tag{5}$$

where q^2 is the sum of the squares of the velocities.

Under the thin-layer approximation, the shear stress and heat transfer terms are contained in $\hat{H}_v$, as below:

$$\hat{H}_v = \frac{M_\infty}{Re_L}\frac{\mu}{J}\begin{bmatrix} 0 \\ \phi_1 u_\zeta + \zeta_x \phi_2 \\ \phi_1 v_\zeta + \zeta_y \phi_2 \\ \phi_1 w_\zeta + \zeta_z \phi_2 \\ \phi_1\left[\dfrac{q^2}{2} + \dfrac{c^2}{P_r(\gamma - 1)}\right]_\zeta + W\phi_2 \end{bmatrix} \tag{6}$$

where

$$\phi_1 = \zeta_x^2 + \zeta_y^2 + \zeta_z^2 \tag{7}$$

$$\phi_2 = (\zeta_x u_\zeta + \zeta_y v_\zeta + \zeta_z w_\zeta)/3 \tag{8}$$

and Pr is Prandtl number, M_∞ is freestream Mach number, and Re_L is Reynolds number evaluated at freestream conditions based on a characteristic body length. The above equations are nondimensionalized with reference values of length, density, speed of sound, and viscosity, i.e., L^*, ρ^*, c^*, μ^*, respectively. The Stokes hypothesis for bulk viscosity and Sutherland's law for molecular viscosity are used for the laminar computations of the present investigation.

The concept of conical similarity is exact for supersonic inviscid flows over conical bodies, but it has also been used to derive an approximate set of viscous equations known as the conical Navier-Stokes equations. The approximation is motivated by the observation that many experimental flows at supersonic speeds demonstrate approximate self-similarity. A length-scale dependence remains in the viscous equations which prevents conical self-similarity; the equations may be thought of as locally conical, where the local Reynolds number is evaluated at the location corresponding to the conical solution. In the present scheme, a single array of crossflow volumes is constructed such that the inflow and outflow planes are surfaces of constant ξ.[18] At each iteration, the inflow conditions are updated with the results of the previous iteration so that at convergence, $\partial Q/\partial \xi = 0$, consistent with the conical property that flow variables remain invariant along rays from the origin. The conical assumption reduces the spatial dimension by one, and consequently, the computing times are much smaller than a fully three-dimensional computation, thereby enabling extensive parametric and design studies to be conducted.[10–12]

Numerical Method

The equations are solved with a finite-volume algorithm in which the spatial and temporal discretizations are uncoupled,

similar to that used previously.[17,18] The convective and pressure terms are upwind-differenced using the flux-difference-splitting scheme of Roe, and the shear stress and heat transfer terms are centrally differenced. The resulting algorithm is second-order accurate in the spatial direction on uniform grids.

The convective and pressure terms are differenced using the monotone upstream-centered schemes for conservation laws (MUSCL) approach of Van Leer. The interface flux is constructed from a state variable interpolation and a locally one-dimensional model of wave interactions normal to the cell interface. The flux-difference-splitting model leads to an interface flux in the ξ-direction, for instance, as

$$\hat{F}_{i+1/2} = \tfrac{1}{2}[\hat{F}^R + \hat{F}^L - |\hat{A}|(Q^R - Q^L)]_{i+1/2} \tag{9}$$

where the subscripts j, k are constant and omitted for presentation. The state-variable interpolations determine the resulting accuracy of the scheme; the state variables at the interface are constructed from nonoscillatory interpolation of the primitive variables $q = (\rho, u, v, w, p)^T$, as

$$(q^L)_{i+1/2} = q_i + \tfrac{1}{2}(\delta^L q)_i \tag{10}$$

$$(q^R)_{i-1/2} = q_i - \tfrac{1}{2}(\delta^R q)_i \tag{11}$$

The interpolation for a component z of the solution vector can be written as

$$(\delta^L z)_i = I(z_{i+1} - z_i, z_i - z_{i-1}) \tag{12}$$

$$(\delta^R z)_i = I(z_i - z_{i-1}, z_{i+1} - z_i) \tag{13}$$

$$I(x, y) = \frac{x(y^2 + 2\varepsilon^2) + y(2x^2 + \varepsilon^2)}{2x^2 - xy + 2y^2 + 3\varepsilon^2} \tag{14}$$

where I is designed to recover the state variable to third-order accuracy in the one-dimensional case in smooth regions of the flow, and interpolate without oscillations near discontinuities in the solution, such as shock waves. The parameter ε^2 is a small constant on the order of the cube of the grid spacing which is used to improve the accuracy near smooth extrema and reduce the nonlinearity of the interpolation in regions of small gradients, such as encountered near the freestream. Where the gradients are small with respect to ε^2, the interpolation without any limiting is recovered.

The backward-time approximation in delta form is given as

$$(\Delta\hat{Q}/\Delta t) + L(\hat{Q}^{n+1}) = 0 \tag{15}$$

where $L(\hat{Q}^n)$ is the discrete representation of the spatial derivative terms in Eq. (1) evaluated at time level n. The equations are linearized with respect to the primitive variables in order to be consistent with the state variable interpolations

$$\left[\frac{M}{J\Delta t} + \frac{\partial L}{\partial q}\right]\Delta q = -L(\hat{Q}^n) \tag{16}$$

The above equation is spatially factored and solved as a series of sweeps through the mesh:

$$L_\xi L_\eta L_\zeta[\Delta q] = -L(\hat{Q}^n) \tag{17}$$

$$q^{n+1} = q^n + \Delta q \tag{18}$$

The implicit spatial derivatives of the convective and pressure terms are taken as first-order upwind differences, leading to tridiagonal inversions for each sweep. The inviscid split-Jacobian matrices used correspond to those arising from similarity transformations. In the ξ and η directions, the block inversions are simplified to scalar inversions using a diagonal approximation. The algorithm is conditionally stable and optimal convergence is usually obtained with a spatially varying time step corresponding to a Courant number on the order of 10.

The solutions in cases not otherwise noted were impulsively stated from freestream initial conditions. On the body, no-slip and adiabatic wall conditions were applied. Freestream conditions were applied on those inflow outer boundaries which are not conical-inflow surfaces. At the downstream outflow boundary, first-order extrapolation boundary conditions were used. The computational cut in the domain for solutions with no symmetry imposed was located on the leeward plane of the body; across this cut, continuation boundary conditions were applied and periodic tridiagonal matrix solutions were used for the implicit equations arising from the time discretization.

Results and Discussion

Conical Flows

The effects of Reynolds number on the sectional side force over a 5-deg half-angle cone at a freestream Mach number of 1.8 and angle of attack of 20 deg using the conical Navier-Stokes equations are shown in Fig. 1. The results are computed on a body-fitted grid with a range of grid densities, with the coarsest grid density consisting of 97 points circumferentially, and 51 points normal to the body. On the coarsest grid, the side force variation is zero (corresponding to symmetric flow) below a critical Reynolds number of approximately 30,000 based on the streamwise length from the nose of the body. A bifurcation to either of two mirror-image asymmetric states appears above this critical Reynolds number. The departure to asymmetry can be classified as an absolute instability of the symmetric flow, since the asymmetries could be triggered in the present computations through a transient asymmetry, arising, for instance, from round-off, or through an initial transient in sideslip, in agreement with previous results of Siclari and Marconi.[10] Note that either of the two mirror-image asymmetric states can be computed and are stable to small disturbances. If a major imposed asymmetry were introduced to change the sign of the asymmetry, from imposed left-right to right-left, for instance, the right-left asymmetry would remain if the imposed asymmetry was removed.

To map out the variation with Reynolds number, the solutions at lower Reynolds numbers were restarted from an existing solution at a higher Reynolds number. The calcula-

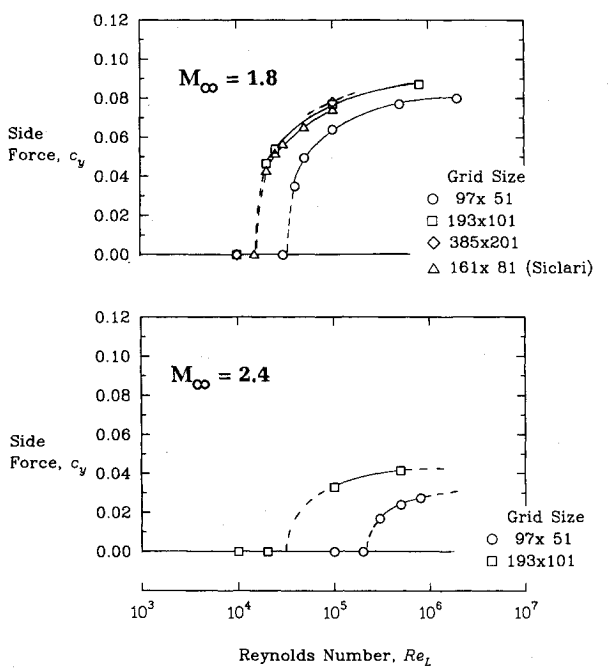

Fig. 1 Effect of Reynolds number on asymmetries computed with conical flow equations.

tions converged very slowly near the critical Reynolds number in comparison to the convergence either above or below the critical Reynolds number. As the Reynolds number is increased, the sectional side force approaches a limiting value, corresponding to a maximal asymmetry.

The finer grid calculations shown in Fig. 1 indicate a decrease in the critical Reynolds number and an increase in the sectional side force as the grid is refined. The computations on the two finer grids of the present study indicate a grid-independent critical Reynolds number of slightly greater than 10,000. The finer grid results are also in good agreement with central-difference computations of Siclari[19] on a 161 × 81 grid.

The effect of increasing the freestream Mach number to 2.4 is also shown in Fig. 1 for computations on the 97 × 51 and the 193 × 101 grids. The effect of increasing Mach number is to decrease the magnitude of the sectional side force and to increase the value of the critical Reynolds to approximately 20,000. The results are in agreement with the conical results of Siclari[11] which indicate that only symmetric flows occur above a Mach number of 3.0 for the 5-deg cone at a Reynolds number of 100,000.

Three-Dimensional Flows

Calculations for the three-dimensional flows were made using two grid topologies. The first approach used a sheared parabolic mapping[20] to generate a grid which extended upstream of the body nose, and blended into a conical grid downstream near the end of the cone, as shown in Fig. 2. The second approach used a conical grid which extended to a region just downstream of the nose. At this inflow boundary, a locally conical boundary condition was applied.

A three-dimensional computation for a Mach number of 1.8 was made at a Reynolds number based on the length of the cone of 100,000 and the same angle of attack as above. In order to minimize the computational work, the crossflow grid density corresponds to the coarsest (97 × 51) grid used in the conical flow solutions. In the direction along the body, 51 points were used. The results obtained with the 97 × 51 grid are representative of the results obtained on finer grids, and the grid is sufficiently dense to allow asymmetric flowfields to develop in the crossflow planes for the three-dimensional case. Entropy contours at several cross-sectional slices through the grid are shown in Fig. 3. The downstream contours show two primary and two secondary vortices as ex-

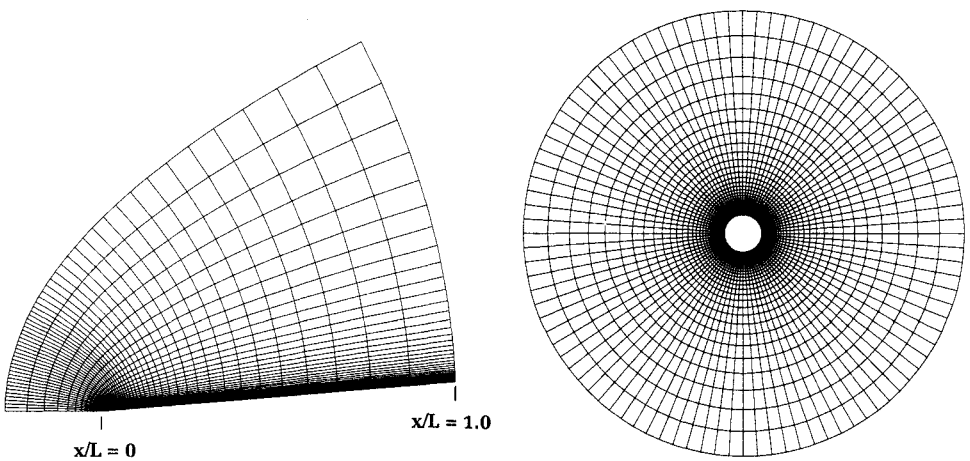

Fig. 2 Longitudinal symmetry plane grid (left) and crossflow plane grid (right) based on sheared parabolic mapping.

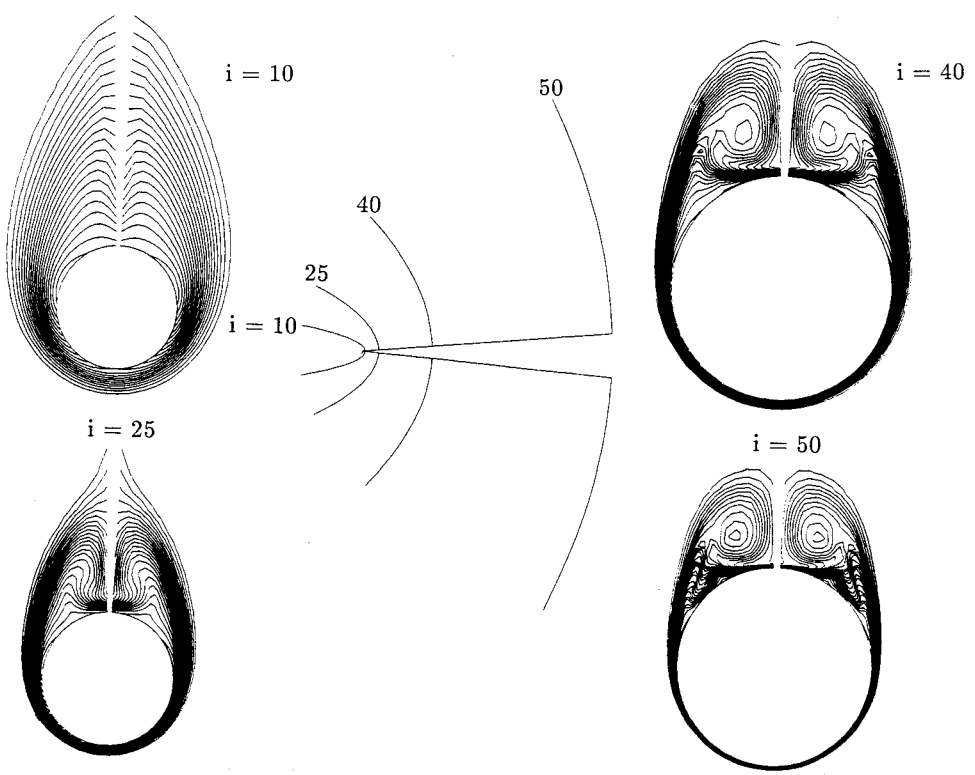

Fig. 3 Longitudinal development of the three-dimensional vortical flow over the cone; cross sections are not to scale.

pected. However, the flow upstream is characterized by a thick boundary layer on the windward side with a diffuse leeward separation region which rolls up into concentrated vortices downstream. It was initially expected that an asymmetry would apear in the three-dimensional calculations, much as with the conical flow solutions. However, the calculations converged to the symmetric solution over the length of the body with no evidence of asymmetry. Also, a sideslip angle was introduced as an initial transient to induce an asymmetry; the flow returned to symmetry following the transient.

The conical flow solutions indicated the existence of a critical Reynolds number, below which the flowfield was always symmetric. In order to check the validity of the conical flow assumption, pressure coefficient as a function of circumferential angle is shown in Fig. 4 for three axial positions from the three-dimensional calculation, as compared to three separate conical flow solutions. Each conical solution was computed with lateral symmetry imposed and with a local Reynolds number based on the distance from the nose of the body to the corresponding streamwise location. The pressures indicate a substantial viscous interaction down the length of the body and the conical flow solutions are nearly identical to the three-dimensional results. The differences are largest at the most upstream station where the viscous interaction is most dominant. Thus, the conical flow assumption is locally a very accurate model for the steady symmetric behavior of the three-dimensional flow.

On the basis of the conical flow solutions, the flowfield in the immediate vicinity of the nose is expected to be viscous-dominated, and therefore, steady and symmetric. The absolute instabilities obtained with the conical flow solutions would indicate asymmetric flow should occur downstream of the critical Reynolds location, corresponding to roughly $0.3x/L$ for this case using the crossflow 97 × 51 grid density (Fig. 1). However, in the conical flow model, there are no state-variable gradients along straight-line generators from the nose; in the present numerical procedure this is implemented by imposing the upstream boundary data at each new iteration as the solution from the last iteration. Hence, any departure from symmetry is immediately imposed as both upstream and downstream boundary data in the computations.

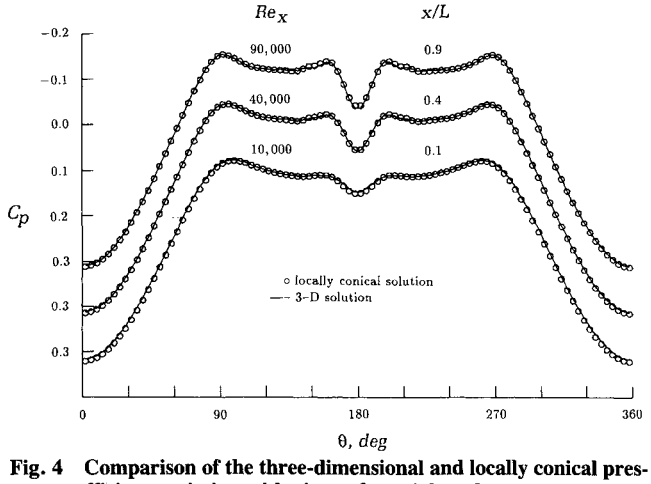

Fig. 4 Comparison of the three-dimensional and locally conical pressure coefficient variation with circumferential angle.

In the three-dimensional case, any departure from asymmetry where the flow is supersonic must propagate downstream inside of the Mach cone. At a given axial location, at each new iteration, the asymmetrical flow is convected downstream and the symmetric flow emanating from the viscous dominated solution at the nose serves as a continuous upstream condition for the predominantly supersonic downstream flow, and suppresses any tendency for the downstream flow to become asymmetric. Thus, the three-dimensional propagation of an asymmetry is fundamentally different from the instantaneous propagation with iteration possible in the conical flow model. As a result, the three-dimensional solution is more stable than that indicated by the locally conical flow model.

As a test of this hypothesis, parametric three-dimensional solutions were made using the conical grid and the upstream locally-conical boundary condition. The solution at a Mach number of 1.8 and Reynolds number of 800,000 was computed at an angle of attack of 20 deg. The crossflow grids were as stated above; the streamwise grids contained 26 points, one with an equal distribution of points and the other with a cosine distribution of points clustered in the nose region. The grid with the equal distribution of points resulted in the first computed cross-sectional plane being in the supercritical region; the first cross-sectional plane with the clustered grid corresponds to the subcritical region. The variation of sectional side force vs longitudinal distance for the two solutions and the entropy contours at the end of the body are shown in Fig. 5. Along with the entropy contours at the end of the body, a front view of the surface grid is shown; the break in the entropy contours above the body represents the computational cut in the grid along which continuation was enforced. The equally spaced grid gives rise to a flowfield which exhibits a noticeable asymmetry from the first streamwise cross section and amplifies downstream. This asymmetry is spurious and occurs because the solution procedure in the nose region is virtually identical to a locally conical flow model, and the

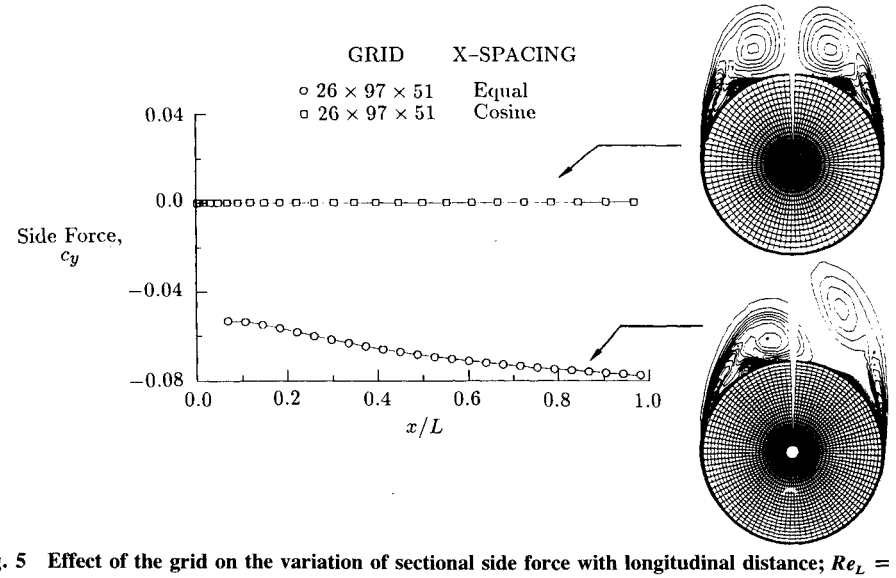

Fig. 5 Effect of the grid on the variation of sectional side force with longitudinal distance; Re_L = 800,000.

asymmetry develops similarly. The clustered grid has a much better resolution in the nose region and gives rise to a symmetrical solution. As a further test, the computation with the clustered grid was restarted from the spurious asymmetrical solution corresponding to the equally spaced grid; the flowfield returned to the same steady symmetric flowfield obtained by impulsively starting from freestream. Therefore, inadequate resolution of the nose region can give rise to a spurious asymmetry. The symmetric solutions obtained with this conical grid agree to plotting accuracy with the solutions obtained using the three-dimensional grid shown in Fig. 4.

Parametric investigations of geometric variations to the nose region were investigated with the clustered grid used above. The circular cross section was modified to an elliptical cross section rotated 45 deg in the circumferential direction over the region upstream of $x/L = 0.004$, as shown in Fig. 6, which is similar to that used in the computational investigation of Hartwich et al.[13] The maximum major-minor axis ratio $(a/b)_{max}$ is 1.25. The sectional side force variation with longitudinal distance for various Reynolds numbers is shown in Fig. 7. The geometrical perturbation causes a departure from symmetry in the nose region. A general trend determined from the variations in Reynolds number is that the asymmetry damps downstream until the critical Reynolds number [denoted as $(x/L)_{crit}$ in the figure] is reached, and then amplifies downstream of that point. The sideforce of the highest Reynolds number solution amplifies quickly and reaches a nearly constant negative sectional side force variation along the body at a level approximately equal to that obtained from the conical flow model.

At the lowest Reynolds number of 30,000, corresponding to the critical Reynolds number associated with the crossflow grid density, the flowfield has returned to symmetry at the end of the body. At a Reynolds number of 100,000, the negative side force caused by the asymmetry exhibits the start of a damped oscillation to symmetry. At the point at which the critical Reynolds number is reached ($x/L = 0.3$), the side force has switched signs from negative to positive; from the critical point, the side force then amplifies slowly downstream so that a positive sectional side force results at the end of the

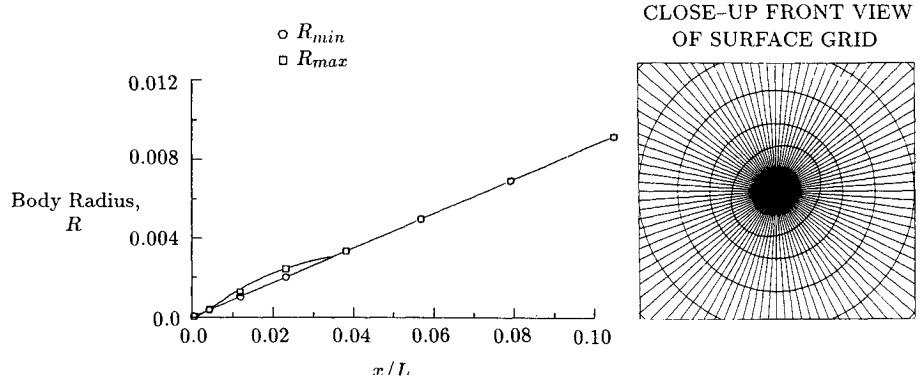

Fig. 6 Variation of maximum and minimum body radius with longitudinal distance for the local geometric asymmetry in the nose region.

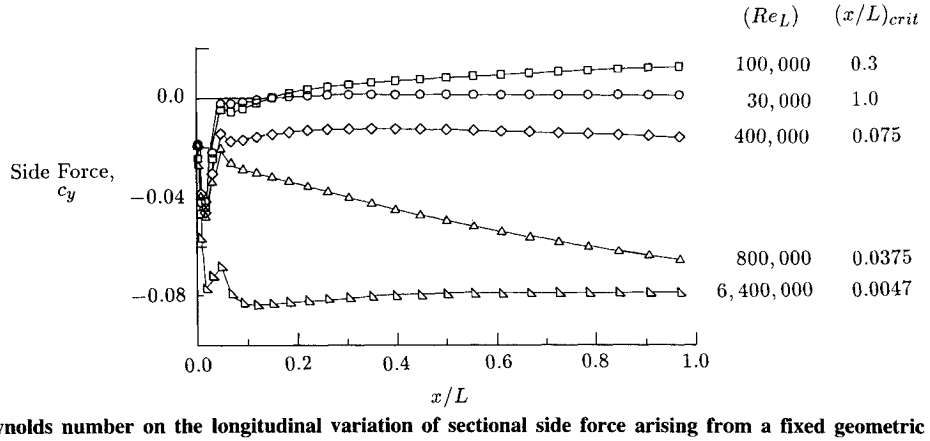

Fig. 7 Effect of Reynolds number on the longitudinal variation of sectional side force arising from a fixed geometric asymmetry in the nose region.

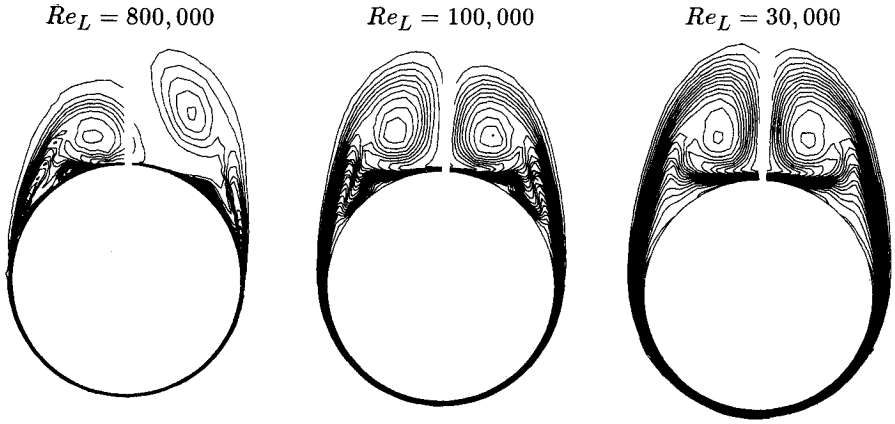

Fig. 8 Effect of Reynolds number on entropy contours at $x/L = 1$ arising from a fixed geometrical asymmetry in the nose region.

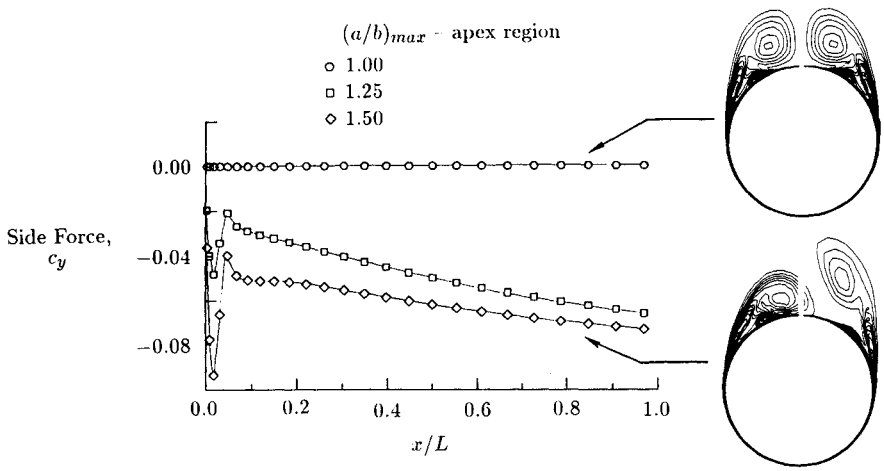

Fig. 9 Effect of the size of the geometric asymmetry on the longitudinal variation of sectional side force at Re_L = 800,000; entropy contours at x/L = 1 are shown for a/b = 1.0 and 1.5.

body. Entropy contours at the downstream locations for three of the Reynolds numbers are shown in Fig. 8, corresponding to the large-negative-side-force, the small-positive-side-force, and the symmetric solution at Reynolds number of 8×10^5, 10^5, and 3×10^4, respectively.

Assuming the imposed geometrical asymmetry can be reversed to give the mirror-image asymmetry to those obtained, the sectional side force downstream spans the range from −0.08 to 0.08. Recalling Fig. 1, the variation in side force is bounded by the sectional side force predictions from the conical flow equations. Thus, given a range of Reynolds numbers with a fixed disturbance, a complete range of asymmetries can be found, which are limited by the asymmetrical high Reynolds conical flow solutions.

The effect of increasing the geometric asymmetry is shown in Fig. 9. At a Reynolds number of 800,000, the sectional side force variation is shown for the symmetric case and two geometrical perturbations which are similar except in the maximum major-minor axis ratio. As expected, the larger perturbation induces a larger asymmetry in the nose region and leads to a larger aymmetry at the downstream station. The amplification rate is similar for the two asymmetric flowfields, but is slightly higher for the smaller perturbation over most of the body length. As in the previous result, the far downstream asymmetry approaches that predicted with the conical equations at this Reynolds number, and a whole range of asymmetries are possible, depending on the magnitude of the geometrical asymmetry.

Conclusions

A definitive computational study of the viscous supersonic flow over a 5-deg cone for a range of Reynolds numbers at an angle of attack of four times the cone half-angle has indicated that:

1) A critical Reynolds number exists below which the flow is always steady and symmetric. Asymmetrical flows which are classified as convective instabilities are found if the local Reynolds number is supercritical and a fixed geometric asymmetry is imposed. Depending on the size of the disturbance and the Reynolds number, a continuous range of asymmetries can be developed. The longitudinal amplification of the asymmetry increases with Reynolds number and the magnitudes of the sectional side force far downstream can be correlated with the side force values predicted using the conical equations. The critical Reynolds number increases and the magnitude of the sectional side force decreases as the Mach number is increased from 1.8 to 2.4.

2) The absolute instabilities of initially symmetric flowfields associated with the solutions to the conical equations do not occur in solutions to the three-dimensional equations. The three-dimensional flow is more stable at a given Reynolds number than the locally conical approximation, and a convective instability is always found. Spurious asymmetric three-dimensional flows for symmetric bodies arise if the grid resolution is insufficient in the nose region. However, the conical flow approximations are extremely useful as limit solutions for three-dimensional asymmetric flows.

It is recognized that the three-dimensional results of the present study apply (strictly speaking) to a single supersonic flow condition. Variations in Mach number and angle of attack remain to be investigated.

References

[1]Keener, E., and Chapman, G. T., "Onset of Aerodynamic Side Forces at Zero Sideslip on Symmetric Forebodies at High Angles of Attack," AIAA Paper 74-770, Aug. 1974.

[2]Peake, D. J., Owen, F. K., and Higuchi, H., "Symmetrical and Unsymmetrical Separations About a Yawed Cone," High Angle of Attack Aerodynamics, AGARD CP 247, Paper 16, Sanderford, Norway, Oct. 1978.

[3]Hall, R. M., "Influence of Reynolds Number on Forebody Side Forces for 3.5-Diameter Tangent-Ogive Bodies," AIAA Paper 87-2274, Aug. 1987.

[4]Hall, R. M., "Forebody and Missile Side Forces and the Time Analogy," AIAA Paper 87-0327, Jan. 1987.

[5]Moskovitiz, C. A., Hall, R. M., and DeJarnette, F. R., "Effects of Surface Perturbations on the Asymmetric Vortex Flow over a Slender Body," AIAA Paper 88-0483, Jan. 1988.

[6]Zilliac, G., and Degani, D., "Asymmetric Vortices on a Slender Body of Revolution," AIAA Paper 90-0388, Jan. 1990.

[7]Degani, D., and Tobak, M., "Numerical, Experimental, and Theoretical Study of Convective Instability of Flows over Pointed Bodies at Incidence," AIAA Paper 91-0291, Jan. 1991.

[8]Fiddes, S. P., "Separated Flow Around Cones at Incidence—Theory and Experiment," *Proceedings of Symposium on Studies of Vortex Dominated Flows*, NASA Langley Research Center, Hampton, VA, July 1985, pp. 285–310.

[9]Marconi, F., "Asymmetric Separated Flows About Sharp Cones in a Supersonic Stream," *Proceedings of the 11th International Conference on Numerical Methods in Fluid Dynamics*, Williamsburg, VA, June–July 1988, pp. 395–402.

[10]Siclari, M. J., and Marconi, F., "The Computation of Navier-Stokes Solutions Exhibiting Asymmetric Vortices," AIAA Paper 89-1817, June 1989.

[11]Siclari, M. J., "Asymmetric Separated Flows at Supersonic Speeds," AIAA Paper 90-0595, Jan. 1990.

[12]Kandil, O., and Wong, T. C., "Prediction of Steady and Unsteady Asymmetric Vortical Flow Around Cones," AIAA Paper 90-0598, Jan. 1990.

[13]Hartwich, P. M., Hall, R. M., and Hemsch, M. J., "Navier-Stokes Computations of Vortex Asymmetries Controlled by Small Surface Imperfections," AIAA Paper 90-0385, Jan. 1990.

[14]Degani, D., and Schiff, L. B., "Numerical Simulation of the Effect of Spatial Disturbances on Vortex Asymmetry," AIAA Paper 89-0340, Jan. 1989.

[15]Degani, D., "Numerical Investigation of the Origin of Vortex

Asymmetry," AIAA Paper 90-0593, Jan. 1990.
[16]Huerre, P., and Monkewitz, P. A., "Local and Global Instabilities in Spatially Developing Flows," *Annual Review of Fluid Mechanics*, Vol. 22, 1990, pp. 473–537.
[17]Thomas, J. L., Krist, S. L., and Anderson, W. K., "Navier-Stokes Computations of Vortical Flows over Low Aspect Ratio Wings," *AIAA Journal*, Vol. 28, Feb. 1990, pp. 205–212.
[18]Thomas, J. L., and Newsome, R. W., "Navier-Stokes Computations of Lee-Side Flows over Delta Wings," *AIAA Journal*, Vol. 27, Dec. 1989, pp. 1673–1679.
[19]Siclari, M. J., private communication, Grumman Corporate Research Center, Bethpage, NY, 1990.
[20]South, J. C., Jr., and Keller, J. D., "Axisymmetric Transonic Flow Including Wind-Tunnel Wall Effects," *Aerodynamic Analyses Requiring Advanced Computers*, NASA SP-347, Pt. II, March 1975, pp. 1233–1268.